In-situ and correlative study of dislocation density and deformation mechanisms in Inconel 690

Zhening Yang[a], Rhys Thomas[a], Jack Donoghue[a], Albert Smith[a], Michael Preuss[a,b], Ali Gholinia[a]*
[a] Department of Materials, The University of Manchester, M13 9PL, United Kingdom
[b] Department of Materials Science & Engineering, Monash University, Vic-3800, Australia

Abstract:
In-situ experimental techniques are essential for understanding the deformation evolution of materials by enabling real-time tracking of microstructure changes. This study employs in-situ electron backscatter diffraction (EBSD), high-resolution digital image correlation (HR-DIC), and in-situ neutron diffraction to investigate the deformation mechanism of IN690. The results reveal that the geometrically necessary dislocation (GND) density does not increase during elastic deformation but exhibits a linear increase during plastic deformation when the strain is less than 10%. Initially, during the onset of plastic deformation, GND density primarily accumulates along grain boundaries, with high-density areas developing within grains as deformation progresses. Careful analysis shows that the free surface effect during deformation does not impact GND density measurements. High resolution digital image correlation (HR-DIC) shear strain maps demonstrate local strain heterogeneity, with long and intense slip traces observed near twin boundaries and an increase in number and intensity of slip traces as deformation progresses. In-situ neutron diffraction indicates that the total dislocation density of IN690, which includes statistically stored dislocations (SSD) and remains unchanged during elastic deformation and increases linearly during plastic deformation. The GND density measured by EBSD constitutes less than 7% of the total dislocation density measured by neutron diffraction.

Key words: In-situ EBSD; HR-DIC; In-situ neutron diffraction; deformation; nickel alloy; Geometrically necessary dislocations; Statistically stored dislocations; Dislocation density

*Corresponding author: Ali Gholinia, ali.gholinia@manchester.ac.uk

1. Introduction

Nickel alloys have been widely used in high-performance applications, such as high corrosive nuclear environments, jet engines and gas turbines due to their excellent corrosion and mechanical properties [1-3]. The mechanical properties of alloys are affected by their microstructure and the micromechanics when the materials are exposed to loading that result in plasticity. Therefore, it is necessary to investigate the microstructure during deformation and have a better understanding of deformation mechanisms of materials.

In-situ experiment, which involves observing materials in their operational environment, allows for the direct observation of microstructural changes as they occur. This approach offers significant advantages over traditional experimental analysis, which can only infer deformation mechanisms after the deformation. By employing advanced characterisation tools such as in-situ electron backscatter diffraction (EBSD), X-ray diffraction (XRD) or neutron diffraction, and high resolution digital image correlation (HR-DIC), in-situ experiments provide a detailed understanding of the dynamic processes governing the mechanical performance of alloys [4-7].

In 1953, Nye [8] introduced dislocation density tensor

$$\alpha_{ij} = n\boldsymbol{b}_i\boldsymbol{r}_j. \quad (1)$$

to relates the dislocation density at a point to the Burgers vector and the dislocation lines, where $\boldsymbol{r}$ and $\boldsymbol{b}$ are the unit and Burgers vector of dislocations and n represents the number of dislocations that

intersect a unit area perpendicular to ***r***. Ashby introduced the concepts of geometrically necessary dislocations (GND) and statistically stored dislocations (SSD), with GNDs being associated with lattice curvature, while SSDs do not contribute to lattice curvature [9]. For 2D EBSD, Pantleon used five components of dislocation density tensor, α_{12},α_{13}, α_{21},α_{23},α_{33}, to resolve 88% of GND content and three components α_{i3} to resolve 66% of GND content [10]. Wheeler et al. also used three components α_{i3} to calculate the weighted Burgers vector (WBV) to describe the lattice curvature [11].

Due to the importance of GND to material deformation, it has been widely investigated by EBSD. Birosca et al. [12] The orientation data indicate that below the yield stress, the pre-existing GND and SSD within the grain move towards the grain boundary and form wider width high-intensity GND near the grain boundary. When the applied stress exceeds the yield stress, dislocations are generated and narrower width of high-intensity GND areas are formed along the grain boundary. Zhang et al. [7] used in-situ EBSD to investigate the grain rotation of Cr20Ni80. The lattice of grain is rotated to a certain extent to accommodate more favourable orientation at lower stress and slip systems are activated and Schmid factor becomes lower to stabilise the microstructure.

The application of correlation theories to measure changes in data was first introduced to digital images in 1975 [13]. DIC is based on tracking unique features from a deformed image back to the original reference image. The images are split into small sub-regions, allowing the displacement of features within each sub-region in the deformed image to be cross-correlated with the matching sub-region in the reference image [14]. DIC has been widely used for strain heterogeneity analysis. For instance, the effect of precipitates on strain heterogeneity of nickel based superalloy was analysed by Harte et al [15]. The strain distribution is more localised in material with precipitates whereas the strain distribution is more uniform for material without precipitates. The slip localisation of Inconel 718 was investigated by HR-DIC and 3D EBSD [16]. The slip band location is normally observed in three microstructure configurations: parallel slip near twin boundary, triple junction configuration and slip transmission in between neighbouring different grains. The longest and most intense slip bands form parallel near the twin boundary planes that have either large difference in Young's modulus but medium Schmid factor or a higher Schmid factor but a lower difference in Young's modulus.

Neutron diffraction is extensively utilised for material analysis due to its deep penetration in most materials, enabling the examination of bulk properties and internal structures with minimal surface interference. This stands in contrast to X-rays that have a shallower penetration depth, particularly in materials with high atomic numbers, which can restrict their analysis to surface or near-surface regions [17]. Due to its advantages, neutron diffraction has been used to investigate the dislocation density [18]. Christien et al. used in-situ neutron diffraction to monitor the dislocation density during martensitic transformation in stainless steel. During the martensitic transformation, dislocation density is very high, but it decreases as the temperature increases from room temperature to 1000°C because the martensite is transformed to austinite [18]. The effect of grain size and solute atoms on dislocation density was also investigated using in-situ neutron diffraction. The results showed that dislocation density is higher when the grain size of the alloy is smaller or when there are more solute atoms [5].

The aim of this paper is to give a detailed introduction to the in-situ experiments, including in-situ EBSD, HR-DIC and in-situ neutron diffraction experiment procedure. Nickel alloy Inconel 690 is used as an example material to analyse deformation mechanisms through these in-situ experiments, which reveal the correlation between GND density, local strain, and total dislocation density.

2. Experimental procedure

2.1 Materials

The material used in this experiment is Inconel 690 (IN690) from New Nuclear Manufacturing (NNUMAN). The main strengthening mechanism of this alloy is solution strengthening. The nominal compositions of IN690 are shown in Table 1 [19].

Table 1. The nominal compositions (in weight%) of IN690 [19]

	Cr	Fe	C	Ni
Inconel 690	29.0	9.0	0.025	Bal

2.2 In-situ EBSD

The samples for the in-situ EBSD experiment were shaped into a dog-bone form using electric discharge machining (EDM), illustrated in Fig. 1. They were then ground with silicon carbide abrasive paper of grit sizes 400#, 800#, 1200#, 2400#, and 4000#. After grinding, the samples underwent polishing with 1 mm and 0.25 mm diamond paste. To ensure a scratch-free finish, a final polish with 0.06 μm colloidal silica was applied.

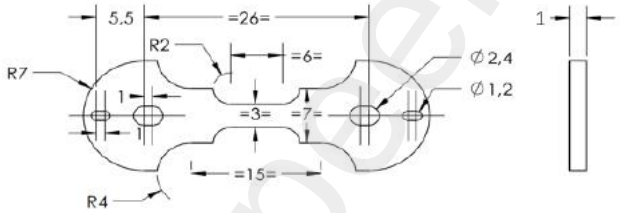

Fig. 1. Sample dimensions for in-situ EBSD.

The polished sample lacked sufficient contrast for tracking region of interest (ROI) automatically and achieving good resolution. To address this, platinum fiducial markers were deposited on the sample surface using a Tescan OptiGIS (Gas Injection System or GIS) fitted in the SEM for in-situ EBSD tracking. This was done by e-beam dissociation of an organometallic gas containing platinum on the sample surface (e-beam deposition). The deposition process used an accelerating voltage of 5 kV and a beam current of 4 nA, taking approximately 15 minutes to complete. These markers enhanced the automatic tracking of the sample's position and focus during the experiment, as shown in Fig. 2.

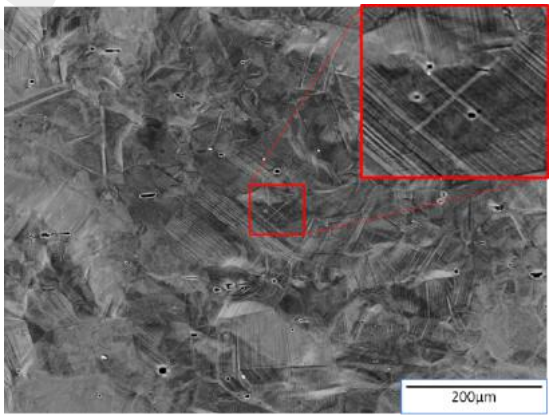

Fig. 2. The SEM image showing the fiducial marker (inside the red square).

Before the in-situ EBSD experiment, the sample was cleaned by Henniker HPT-100, and Evactron plasma cleaner for 5 min and 1 hour respectively to avoid carbon deposition. The in-situ EBSD experiment was carried out using a TESCAN CLARA FEG-SEM equipped with an Oxford Instruments Symmetry S2 EBSD detector. The parameters included an accelerating voltage of 20 kV, a beam current of 10 nA, a working distance of approximately 23 mm, and a step size of 250 nm. The field of view for the IN690 sample was 750 μm × 563 μm. The EBSD was set to Speed 2 mode with a pattern resolution of 156×128 pixels, using optimised band detection for indexing. The exposure time was 0.5 ms. The EBSD settings were consistent during experiment [20].

For the in-situ tensile test, a NewTec MT1000 mechanical loading stage was used, capable of loads up to 5 kN. Fig. 3 shows the EBSD detector on the left and tensile testing rig tilted to 70° on the right. The sample was mounted on the rig as shown as inserted in Fig. 3. The NewTec Soft Strain software facilitated full automation of the testing and image capture processes, along with control of both the in-situ stage and the microscope. Preloading was set at 100 N, with the alloys loaded at a rate of 1 μm/s at room temperature, and displacement control set to 10 μm per step, resulting in a strain rate of 1.7×10^{-4} /s. There were 80 steps in total.

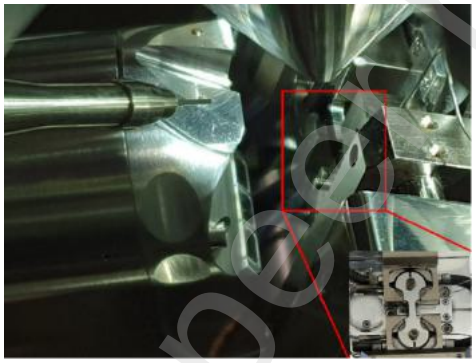

Fig. 3. TESCAN CLARA Scanning Electron Microscope (SEM), NewTec in-situ tensile stage and Symmetry S2 EBSD detector.

At the start of the experiment, a 100 μm × 100 μm field of view was programmed to track the position and perform autofocus. After focusing, the field of view was adjusted to the EBSD mapping area, and the EBSD mapping commenced. Then, a new load was applied, and the procedure was repeated. The in-situ experiment procedures are summarised in Fig. 4. To stabilise the microstructure, the sample was held for 10 minutes after each additional loading step. A minor load relaxation was performed at each step to prevent material relaxation during imaging, keeping the sample as stable as possible without fully unloading.

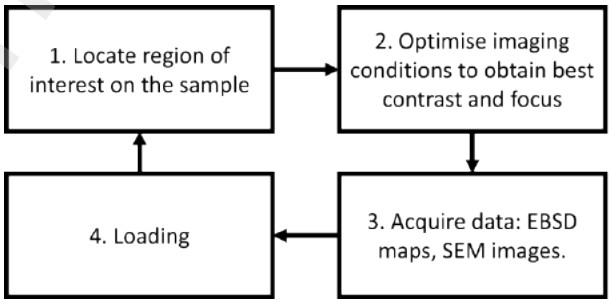

Fig. 4. In-situ experiments procedures.

The GND density is calculated by weighting Burgers vector (WBV) method [21]. The equation is

$$\rho = \frac{W}{bl_3}. \qquad (2)$$

Where W is the magnitude of WBV, b is Burgers vector of nickel. l_3 is the sine of the angle the dislocation line with the map plane. This method uses 3 components α_{i3} of Nye tensor and only 66% of GND density are resolved by this method [10]. However, there is no assumptions about GND types at any stage of calculation [11]. The GND density was calibrated by single crystal silicon to reduce noise from equipment [22].

2.3 HR-DIC

A silver pattern was applied to the polished sample surface. The reason why silver pattern was chosen is that it does not affect the quality of the EBSD map, while other common patterns, like gold, significantly impact the hit rate of the EBSD map.

The coating machine used in this experiment was Quorum coater. A 3 nm titanium layer was deposited onto the sample surface first. The aim of the procedure was to improve the adhesion between the substrate and the subsequent sliver layers. This layer guarantees the adhesion of the coating to the substrate and possesses adequate ductility to deform along with the substrate under significant strains. Titanium, with its elevated surface energy, improves the surface's wettability, leading to a more uniform distribution of the subsequent layers [23, 24]. Subsequently, a 5 nm thickness of a silver pattern was applied to the sample surface at a coating rate of 2-3 nm/min. Following the coating, the samples were immersed in a solution containing 50g of isopropanol and 0.5g of sodium bromide for 3 hours. Fig. 5 shows the silver pattern on the sample surface.

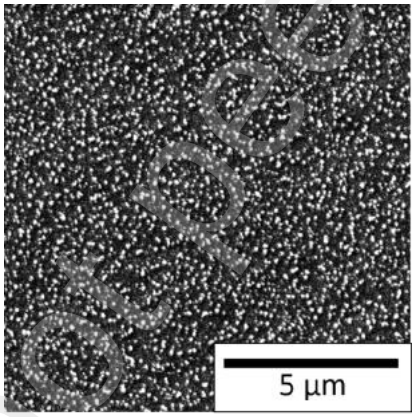

Fig. 5. Silver pattern on IN690 sample surface.

HR-DIC was conducted on the TESCAN CLARA SEM with NewTec MT1000 tensile testing rig. The view field was set as 500 µm × 500 µm. 13 × 13 grids with 50 µm × 50 µm view field was used with overlap of 20%. The accelerating voltage was 5 kV and beam current was 3 nA. There were 35 steps, and the displacement of each step was 30 µm. The strain rate was also 1.7×10^{-4} /s. Similarly to in-situ EBSD, a fiducial marker was also printed on the sample surface to track ROI and focus automatically. Fig. 6 shows a schematic of 10 × 10 grids with 20% overlap.

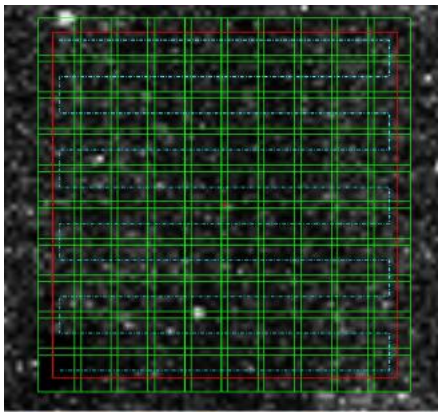

Fig. 6. The schematic of overlap tiles. The green boxes show each individual tile and their overlap. The blue dotted line shows the scan directions. The red box shows the desired view field size.

The 13×13 image grids were stitched to a large image using the Grid/Collection stitching plugin in FIJI software [25]. Consequently, the stitched images were correlated using DaVis 8.4.0 software. The correlation method was integral cross-correlation mode, which means the first stitched image is the reference, and all other images are correlated with this one. The sub-window size was 24 × 24.

The DIC results can be presented be maximum effective in-plane shear strain map as this strain takes all components of the in-plane strain into consideration. Maximum effective shear strain is used. The equation is as follows:

$$\gamma_{max} = \sqrt{\left(\frac{\varepsilon_{xx} - \varepsilon_{yy}}{2}\right)^2 + \left(\frac{\varepsilon_{xy} + \varepsilon_{yx}}{2}\right)^2}. \quad (3)$$

Where ε_{xx} is the strain in loading direction, ε_{yy} is the strain normal to the loading direction, and ε_{xy} is the in-plane shear strain. The DIC data is processed by DefDAP package [26].

2.4 In-situ Neutron diffraction

The schematic of in-situ neutron diffraction is shown in Fig. 7. In-situ neutron diffraction was performed using a Time-of-Flight (TOF) neutron diffractometer, equipped with a slit measuring 4 mm in width, 8 mm in height, and positioned 300 mm away, alongside a 100 kN Instron rig at the ENGIN-X facility within the ISIS facility at Rutherford Appleton Laboratory (RAL, UK). Two band detectors were put at ±90° fixed angle to the incident beam. The d-spacing along the axial direction was measured by bank 1, and the d-spacing perpendicular to it was measured by bank 2. The experiment involved 20 loading steps for each material, applying strain up to 12.8% at a rate of 1.7×10^{-4} /s. Each step required a counting time of at least 20 minutes (24mA/66mA/h).

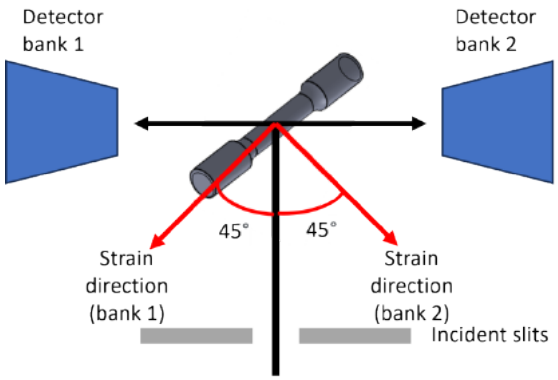

Fig. 7. Schematic of in-situ neutron diffraction. There are two detector banks on ENGIN-X, at ±90° to the incident beam. The sample is positioned at a 45° angle to the incident beam.

For line profile analysis, the experiment utilised a multiple diffraction peak approach provided by the TOF instrument. The analysed neutron diffraction patterns included reflection planes (111), (200), (220), (311), (222), and (400), using the convolutional multiple whole profile (CMWP) method. This method convolves three functions (size, strain, and instrumental profiles), with the background determined separately.

Errors in the analysis stem from the Monte Carlo fitting cycle construction of the CMWP [27]. If a particular weighted sum of square residuals (WSSR) value exceeds the best value ($WSSR_{best}$) found up to that point but is within 3.5% of $WSSR_{best}$, the associated physical parameter values are recorded for error estimation. The largest and smallest values of each parameter within the 3.5% range of $WSSR_{best}$ are considered the plus-minus absolute errors of the respective parameters, as shown in Fig. 8 [28].

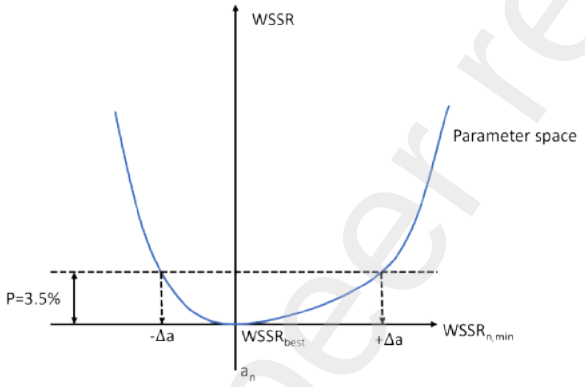

Fig. 8. The errors calculated by CMWP. The confident parameter p=3.5%. The lowest value $WSSR_{best}$ is the result and the values within the 3.5% range of $WSSR_{best}$, -Δa and -Δa, are considered as errors [28].

3. Results

3.1 GND density measured by in-situ EBSD

Fig. 9 illustrates the GND maps of IN690 at different strain levels. It shows the evolution of GND density changes as deformation progresses. During the early stage of plastic deformation from 0% to 2%, there are only a few areas where GND density increases. These areas are mainly near the grain boundary or triple points. When the strain increases from 2% to 4%, there are more areas near the grain boundary with higher GND density. As the strain increases from 4% to 10%, apart from the areas near the grain boundary, there are some areas with high GND density inside the grains.

Fig. 10 shows the change in GND density with increasing strain. During elastic deformation, the GND density of IN690 does not change, indicating that there is no generation of GND. The elastic strain is caused by temporary displacement of atoms from their equilibrium positions. During plastic deformation, the GND density increases relatively linearly with the increase of strain.

The grains at the sample surface are not in the out-of-plane direction, unlike the grains within the sample. Consequently, it is assumed that the surface grains behave differently from the grains inside the sample. This phenomenon can lead to the free surface effect. Therefore, it is necessary to investigate whether the free surface affects the GND density measurement by in-situ EBSD. A sample of same IN690 alloy at the strain of 12.8% was cut and polished 4 mm beneath the surface. Fig. 11 shows the GND density of IN690 at the strain of 12.8% at 4 mm below the outer surface. This depth is deep enough to the reduce free surface effect. The GND density measured by this EBSD map is

0.3×10^{14} /m^2. It is expected that the GND density of the alloy deformed in-situ increased in a linear trend. Hence, at a strain of 12.8% the estimated GND density is 0.29×10^{14} /m^2. Therefore, no surface effect in terms of GND density was observed.

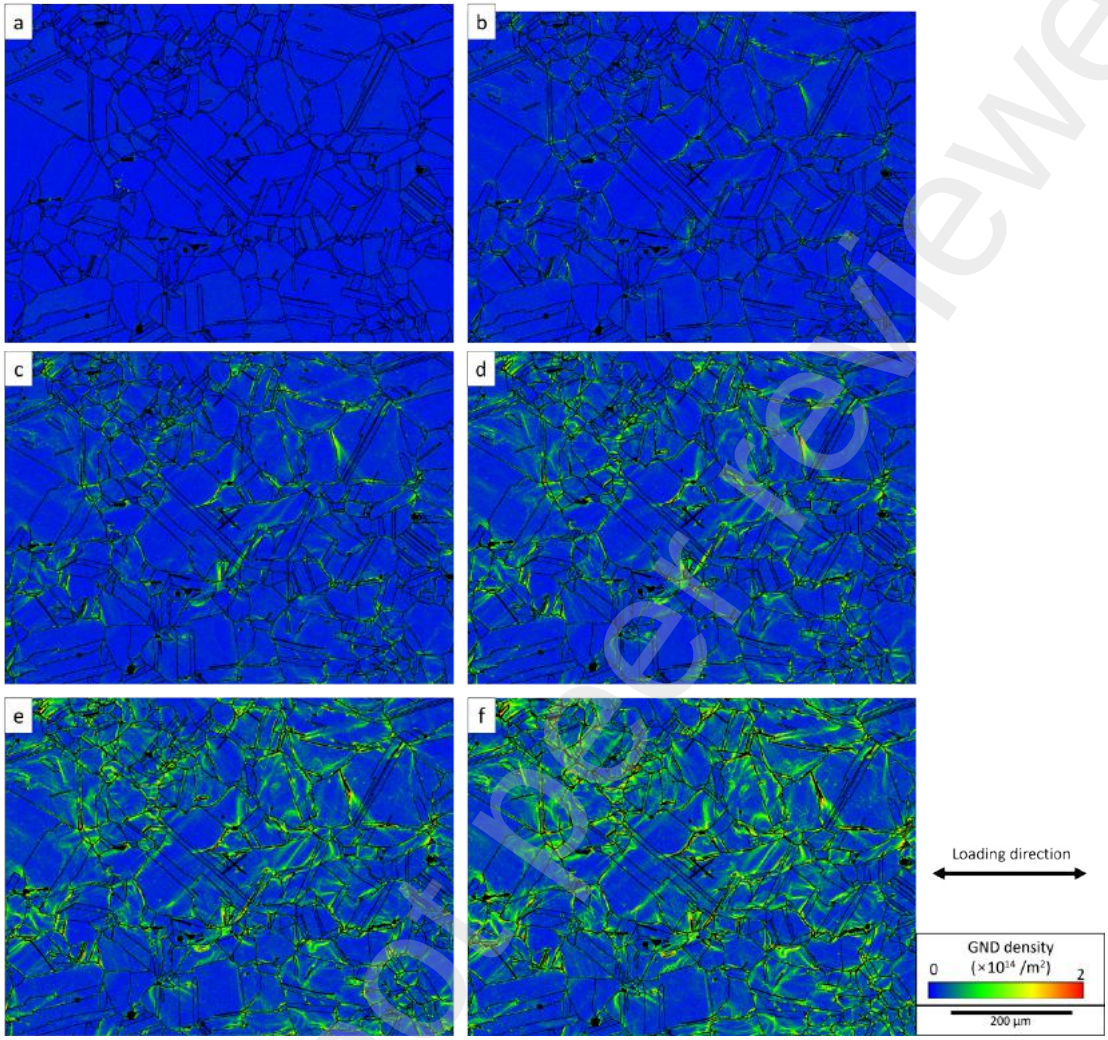

Fig. 9. GND maps of IN690 at strain of 0% (a), 2% (b), 4% (c), 6% (d), 8% (e), 10% (f).

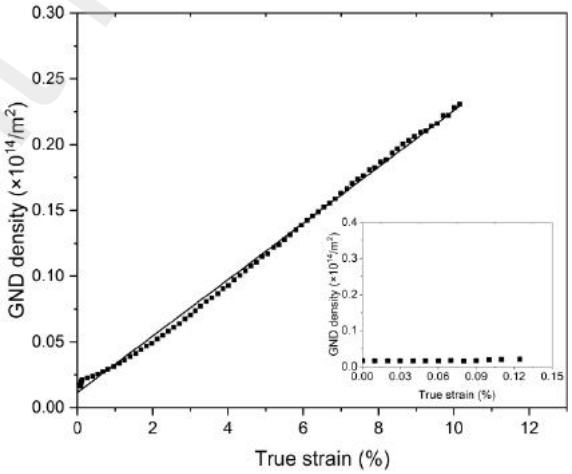

Fig. 10. GND density change of IN690 as strain increases. A linear line is fitted to these points. The inserted figure shows the GND density of IN690 during elastic deformation.

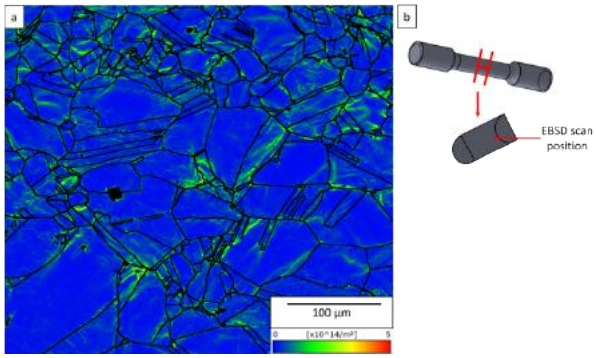

Fig. 11. (a) GND density of IN690 at the strain of 12.8%. The measured surface is 4 mm below the outer surface. (b) The schematic of the sample showing the EBSD scan position.

3.2 HR-DIC

Fig. 12 shows the DIC shear strain map of IN690 at effective shear strain of 0%, 2.2%, 4.4%, 6.6%, 8.8%. When the strain increases from 0% to 2.2%, some slip traces can be observed whereas the number of slip traces is limited. There are two areas with high effective shear strain near twin boundaries as highlighted as 'A' and 'B' by red boxes. When the strain increases from 2.2% to 4.4%, there are more slip traces occurring to accommodate such strain level as measured in the DIC maps. The effective shear strain of slip traces is higher compared to that at strain of 2.2%. Similarly, as the deformation progresses, there are more slip traces and the effective shear strain of slip traces increase.

A grain is used to demonstrate the local strain evolution, as shown in Fig. 13. The line profiles at different strain levels are presented in this figure. At a strain of 1.1%, which is at the beginning of plastic deformation, there are seven slip traces with relatively low effective shear strain values. When the strain increases to 2.2%, the number of slip traces rises to eleven in this area. At strain levels of 1.1% and 2.2%, the strain value of each slip trace is nearly the same, as evidenced by the similar peak height of each slip trace.

As the strain increases to 4.4%, new slip traces can be observed in the DIC map. Moreover, it is apparent that some slip traces have higher effective shear strain compared to others, indicating that the strain is starting to become heterogeneous. When the strain reaches 6.6% and 8.8%, the effective shear strain becomes increasingly heterogeneous. Specifically, the strain is lower on the left side of the grain and does not increase significantly during deformation, whereas the strain becomes progressively higher on the right side of the grain. Additionally, new slip traces can also be seen in the DIC map.

The IPF, GND and DIC maps of this grain are shown in Fig. 14. The GND density bands can be observed in the GND map. These GND density bands align with the slip trace direction A in DIC map. The slip plane of A is $(\bar{1}11)$. The WBV of each data point in these two GND density areas is shown in Fig. 14 (c). The WBV direction is quite similar within each slip plane. WBV integral loops are drawn, with single red arrows indicating the direction of the Burgers vector loop. The WBV direction for A is near <212>, which is close to the <110> FCC slip direction. The slight difference is caused by the weighted variable contribution of different <110> slip directions in different data points.

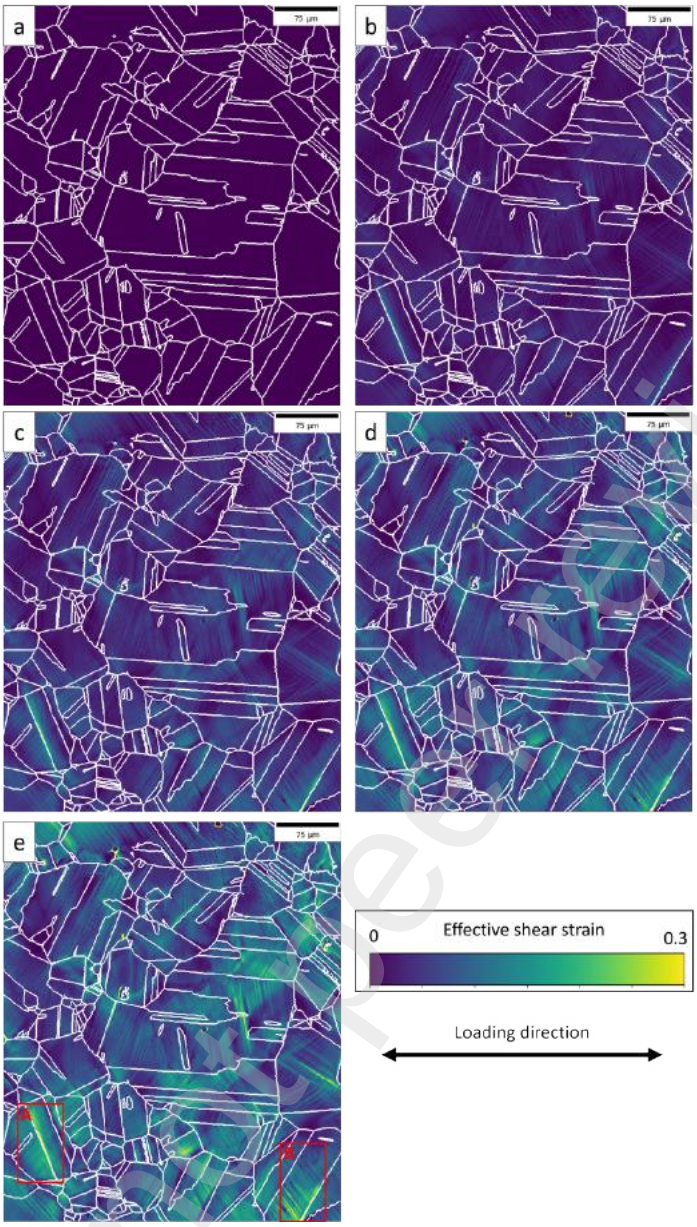

Fig. 12. DIC maps of IN690 at different effective shear strain levels: 0% (a), 2.2% (b), 4.4% (c), 6.6% (d), 8.8% (e).

When the effective shear strain is 8.8%, the area near the twin boundary, marked as A and B in Fig. 12, has a very high local strain. This type of strain localisation can also be seen in [16, 29]. Fig. 15 shows the EBSD IPF colour orientation, Schmid factor and Young's modulus maps, where twin boundaries exhibit intense local strain, as observed in the DIC map. From the EBSD maps of grains in Fig. 15 (a, b, c), the Schmid factor of grain A is 0.44, Schmid factor of grain B is 0.45. The Young's modulus of grain A is 228 GPa, while Young's modulus of grain B is 181 GPa. However, for the grains in Fig. 15 (d, e, f), the Schmid factor of grain C is 0.49, Schmid factor of grain D is 0.48. The Young's modulus of grain C is 213 GPa, while Young's modulus of grain D is 191 GPa. From the literature, the most intense and longest slip bands are found along twin planes that either show a significant difference in elastic modulus with a moderate Schmid factor, or a high Schmid factor with a smaller difference in elastic modulus. Overall, The Schmid factor has an inverse relationship to the difference in Young's modulus [16, 30, 31]. In the first grain, the Schmid factor of the neighbouring grain is smaller while the Young's modulus difference is larger, whereas in the second grain, the Schmid factor is high while the Young's modulus difference is small. This is the reason why high local strain can be seen near these twin boundaries.

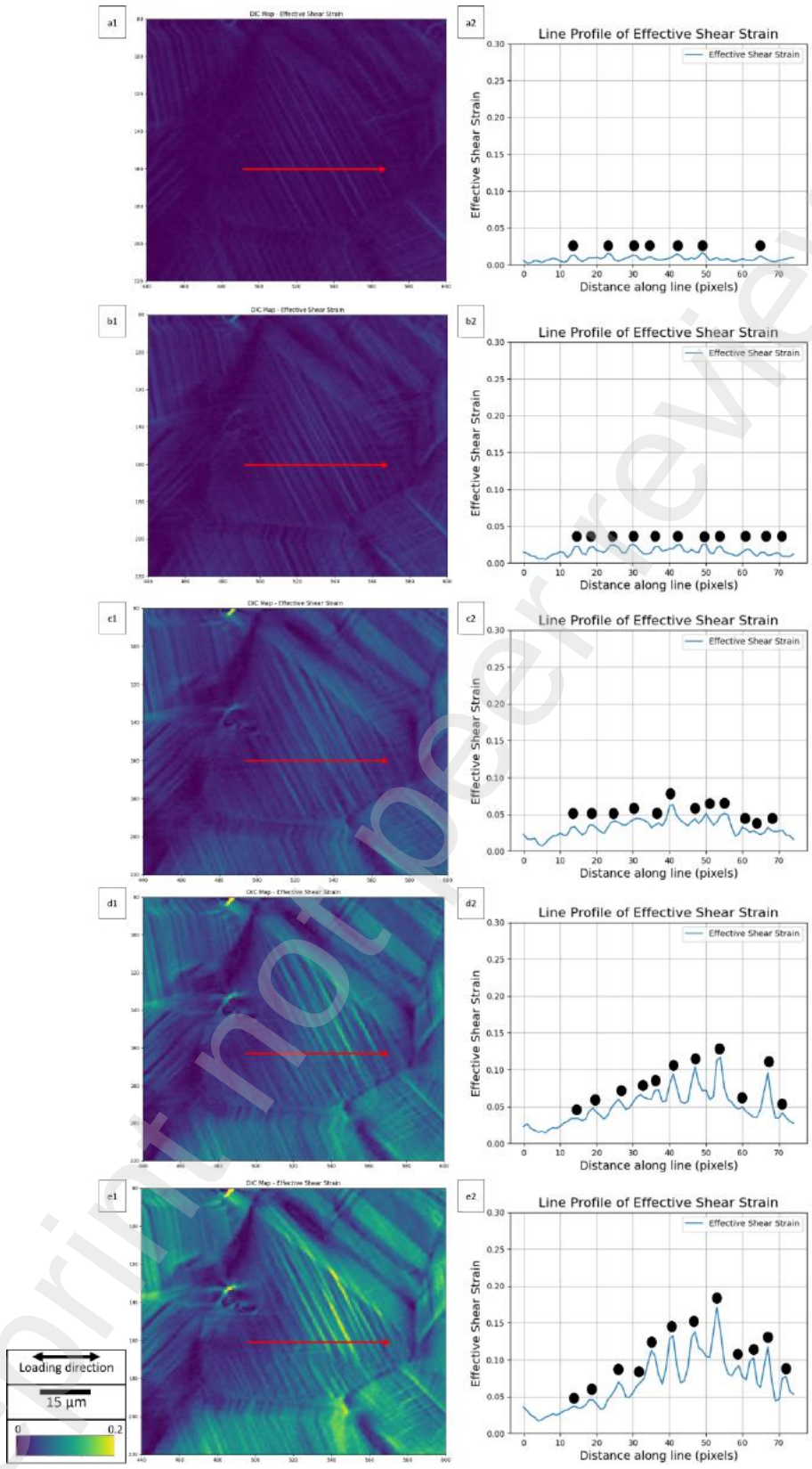

Fig. 13. DIC maps of an example grain at strain levels of 1.1% (a1), 2.2% (b1), 4.4% (c1), 6.6% (d1), and 8.8% (e1). A line profile is drawn as red arrow inside the grain at each strain level. The effective shear strain along the line profile is shown in (a2)–(e2). Black circles show the peaks of slip traces. Yellow arrow A and B indicate two slip trace directions.

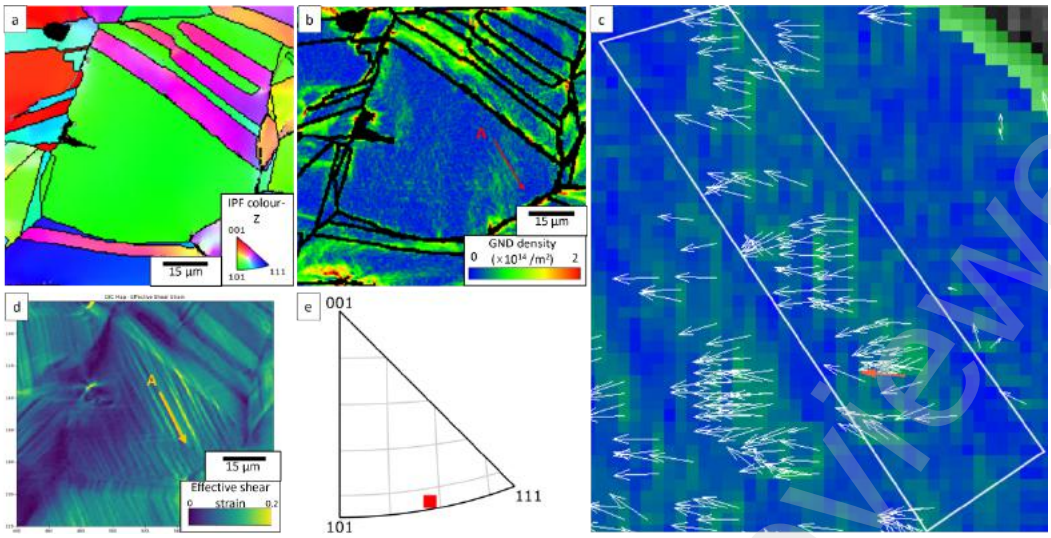

Fig. 14. IPF map (a) and the GND density map (b) of the example grain at effective shear strain of 8.8%. Direction A indicates the GND density band along the slip trace direction. (c) shows the direction of WBV of each data point in the A area. White boxes are WBV loops. The red arrow is the direction of the net Burgers vector for the loops. (d) is DIC map of this grain. (e) is the WBV of area A in crystal coordinates.

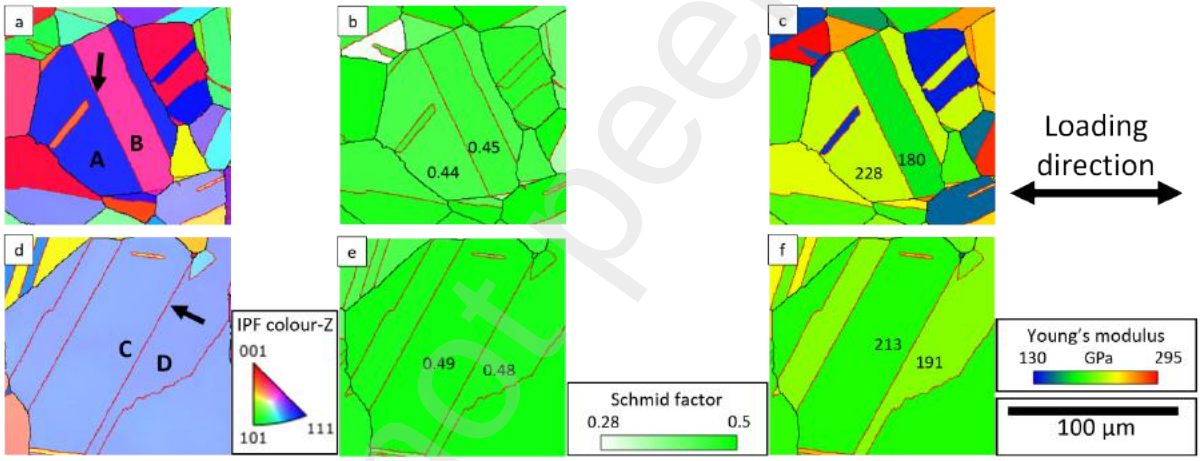

Fig. 15. EBSD maps showing inverse pole figure (IPF) (a, d) Schmid factor (b, e) and Young's modulus (c, f) of grains that have high local strain near the twin boundaries. Twin boundaries are highlighted by red colour. The twin boundaries that have intense local strain in DIC map are shown by black arrows.

3.3 In-situ neutron diffraction

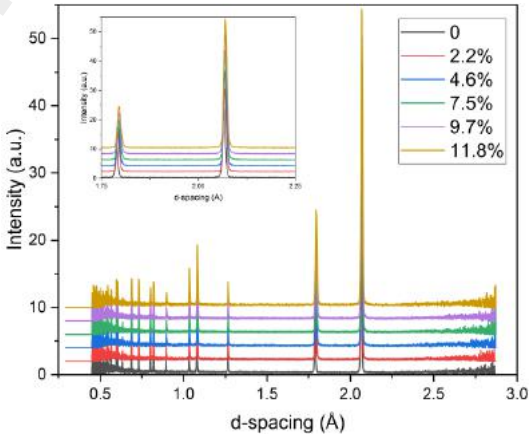

Fig. 16. Neutron diffraction pattern of IN690 at the strain of 0, 2.2%, 4.6%, 7.5%, 9.7%, 11.8%. The inserted figure shows two peaks on the right.

Fig. 16 shows the neutron diffraction pattern of IN690 at the strain of 0, 2.2%, 4.6%, 7.5%, 9.7%, 11.8%. during deformation, the diffraction peak is broader due to the heterogeneous lattice strain, which is more obvious in the inserted figure. The total dislocation density can be calculated using CMWP, from the peak broadening of the diffraction peaks in the diffraction spectra. The total dislocation density increase trend is shown in Fig. 17. The total dislocation density does not change during elastic deformation and the total dislocation density has a relatively linear increase during plastic deformation.

Compared to the GND density measured by EBSD, the GND density only accounts for a small percentage of the total dislocation density. Specifically, the GND density measured by EBSD accounts for 7% of the total dislocation density measured by neutron diffraction at the early stages of plastic deformation, while the GND density accounts for only 3% of the total dislocation density at high strain. This is because the GND density measured using the WBV method in 2D EBSD maps represents only 66% of the resolved GND density. Furthermore, 3D EBSD maps are required to capture all GNDs. Moreover, the difference between the total dislocation density and the GND density, which is the SSD density, becomes larger as seen in the logarithmic scale in Fig. 17, indicating that SSDs become the main contributor to the total dislocation density. Ashby [9] showed that the GND density increases linearly with shear strain, whereas the SSD density is nearly proportional to the square of the shear strain. Consequently, the difference between SSD and GND densities will become more pronounced at high strain.

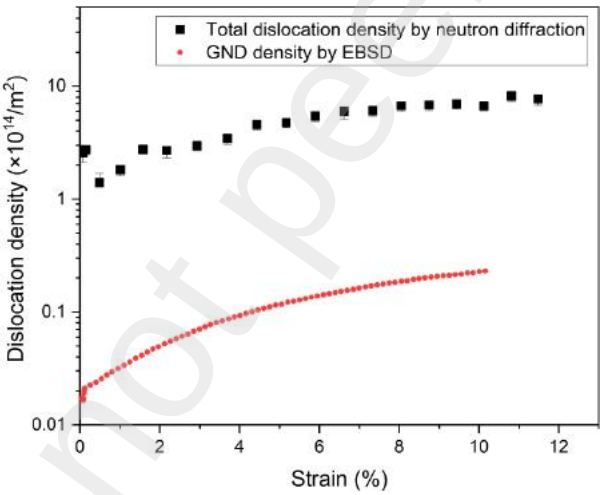

Fig. 17. Total dislocation density of IN690 measured by in-situ neutron diffraction and GND density of IN690 measure by EBSD.

4. Conclusion

In-situ experiments are powerful techniques for investigating the deformation evolution of materials, as the microstructure evolution can be tracked during the experiment. In this paper, in-situ EBSD, HR-DIC, and in-situ neutron diffraction were used to investigate the deformation mechanism of IN690. The results are as follows:

The GND density does not increase during elastic deformation but shows a linear increase during plastic deformation when the strain is less than 10%. Initially, at the beginning of plastic deformation, the GND density mainly accumulates along the grain boundary, with more areas of high GND density appearing within the grains as deformation progresses. The free surface effect during deformation does not affect GND density measurement results.

DIC maps reveal the heterogeneity of local strain. Long and intense slip traces are found near the twin boundary, which is related to the Schmid factor value and Young's modulus difference between

the neighbouring grains. At higher strain, the slip trace number and shear strain intensity of slip traces become higher.

In-situ neutron diffraction shows the total dislocation density of IN690. Similar to the GND density measured by EBSD, the total dislocation density does not change during elastic deformation and increases relatively linearly during plastic deformation. SSDs become more and more significant contributor to total dislocation density as deformation progresses.

5. Reference

[1] E. Akca and A. Gürsel, 'A Review on Superalloys and IN718 Nickel-Based INCONEL Superalloy', *PEN*, vol. 3, no. 1, Jun. 2015, doi: 10.21533/pen.v3i1.43.

[2] G. Gudivada and A. K. Pandey, 'Recent developments in nickel-based superalloys for gas turbine applications: Review', *Journal of Alloys and Compounds*, vol. 963, p. 171128, Nov. 2023, doi: 10.1016/j.jallcom.2023.171128.

[3] M. T. Jovanovi, B. Luki, Z. Miškovi, I. Bobi, I. Cvijovi, and B. Dim, 'PROCESSING AND SOME APPLICATIONS OF NICKEL, COBALT AND TITANIUM-BASED ALLOYS', *JOURNAL OF METALLURGY*.

[4] D. Lunt *et al.*, 'Comparison of sub-grain scale digital image correlation calculated using commercial and open-source software packages', *Materials Characterization*, vol. 163, p. 110271, May 2020, doi: 10.1016/j.matchar.2020.110271.

[5] P. Thirathipviwat *et al.*, 'In-situ neutron diffraction study on a dislocation density in a correlation with strain hardening in Al–Mg alloys', *Materials Science and Engineering: A*, vol. 855, p. 143956, Oct. 2022, doi: 10.1016/j.msea.2022.143956.

[6] W. Q. Gao and A. Godfrey, 'Surface patterning allowing combined EBSD and DIC investigations during in-situ deformation experiments', *Materials Letters*, vol. 308, p. 131272, Feb. 2022, doi: 10.1016/j.matlet.2021.131272.

[7] C. Zhang *et al.*, 'In-situ EBSD study of deformation behavior of nickel-based superalloys during uniaxial tensile tests', *Materials Today Communications*, vol. 35, p. 105522, Jun. 2023, doi: 10.1016/j.mtcomm.2023.105522.

[8] J. F. Nye, 'Some geometrical relations in dislocated crystals', *Acta Metallurgica*, vol. 1, no. 2, pp. 153–162, Mar. 1953, doi: 10.1016/0001-6160(53)90054-6.

[9] M. F. Ashby, 'The deformation of plastically non-homogeneous materials', *The Philosophical Magazine: A Journal of Theoretical Experimental and Applied Physics*, vol. 21, no. 170, pp. 399–424, Feb. 1970, doi: 10.1080/14786437008238426.

[10] W. Pantleon, 'Resolving the geometrically necessary dislocation content by conventional electron backscattering diffraction', *Scripta Materialia*, vol. 58, no. 11, pp. 994–997, Jun. 2008, doi: 10.1016/j.scriptamat.2008.01.050.

[11] J. Wheeler, S. Piazolo, D. J. Prior, P. W. Trimby, and J. A. Tielke, 'Using crystal-lattice distortion data for geological investigations: the weighted Burgers vector method', *Journal of Structural Geology*, vol. 179, p. 105040, Feb. 2024, doi: 10.1016/j.jsg.2023.105040.

[12] S. Birosca *et al.*, 'The dislocation behaviour and GND development in a nickel based superalloy during creep', *International Journal of Plasticity*, vol. 118, pp. 252–268, Jul. 2019, doi: 10.1016/j.ijplas.2019.02.015.

[13] T. J. Keating, 'An Improved Method of Digital Image Correlation', *PHOTOGRAMMETRIC E GINEERING & REMOTE SENSING*, vol. 41, no. 8, pp. 993–1002, 1975.

[14] F. Hild and S. Roux, 'Digital Image Correlation: from Displacement Measurement to Identification of Elastic Properties – a Review', *Strain*, vol. 42, no. 2, pp. 69–80, 2006, doi: 10.1111/j.1475-1305.2006.00258.x.

[15] A. Harte *et al.*, 'The effect of solid solution and gamma prime on the deformation modes in Ni-based superalloys', *Acta Materialia*, vol. 194, pp. 257–275, Aug. 2020, doi: 10.1016/j.actamat.2020.04.004.

[16] M. A. Charpagne *et al.*, 'Slip localization in Inconel 718: A three-dimensional and statistical perspective', *Acta Materialia*, vol. 215, p. 117037, Aug. 2021, doi: 10.1016/j.actamat.2021.117037.
[17] P. L., '3 - Neutron diffraction methods', in *Structural and Residual Stress Analysis by Nondestructive Methods*, V. Hauk, Ed., Amsterdam: Elsevier Science B.V., 1997, pp. 495–521. doi: 10.1016/B978-044482476-9/50017-7.
[18] F. Christien, M. T. F. Telling, and K. S. Knight, 'Neutron diffraction in situ monitoring of the dislocation density during martensitic transformation in a stainless steel', *Scripta Materialia*, vol. 68, no. 7, pp. 506–509, Apr. 2013, doi: 10.1016/j.scriptamat.2012.11.031.
[19] R. C. Reed, *The superalloys: fundamentals and applications*. Cambridge, UK ; New York: Cambridge University Press, 2006.
[20] T. J. Ruggles, T. M. Rampton, A. Khosravani, and D. T. Fullwood, 'The effect of length scale on the determination of geometrically necessary dislocations via EBSD continuum dislocation microscopy', *Ultramicroscopy*, vol. 164, pp. 1–10, May 2016, doi: 10.1016/j.ultramic.2016.03.003.
[21] J. Wheeler, E. Mariani, S. Piazolo, D. j. Prior, P. Trimby, and M. r. Drury, 'The weighted Burgers vector: a new quantity for constraining dislocation densities and types using electron backscatter diffraction on 2D sections through crystalline materials', *Journal of Microscopy*, vol. 233, no. 3, pp. 482–494, 2009, doi: 10.1111/j.1365-2818.2009.03136.x.
[22] Z. Yang, R. Thomas, J. Donoghue, A. Smith, M. Preuss, and A. Gholinia, 'Practical considerations of parameters on GND density measurements by EBSD', *To be published*.
[23] C. B. Montgomery, B. Koohbor, and N. R. Sottos, 'A Robust Patterning Technique for Electron Microscopy-Based Digital Image Correlation at Sub-Micron Resolutions', *Exp Mech*, vol. 59, no. 7, pp. 1063–1073, Sep. 2019, doi: 10.1007/s11340-019-00487-2.
[24] L. Vitos, A. V. Ruban, H. L. Skriver, and J. Kollár, 'The surface energy of metals', *Surface Science*, vol. 411, no. 1–2, pp. 186–202, Aug. 1998, doi: 10.1016/S0039-6028(98)00363-X.
[25] S. Preibisch, S. Saalfeld, and P. Tomancak, 'Globally optimal stitching of tiled 3D microscopic image acquisitions', *Bioinformatics*, vol. 25, no. 11, pp. 1463–1465, Jun. 2009, doi: 10.1093/bioinformatics/btp184.
[26] M. Atkinson, R. Thomas, A. Harte, P. Crowther, and J. Quinta Da Fonseca, 'DefDAP: Deformation Data Analysis in Python - v0.92 (Version 0.92). Zenodo.', 2020.
[27] H. Tyralis, D. Koutsoyiannis, and S. Kozanis, 'An algorithm to construct Monte Carlo confidence intervals for an arbitrary function of probability distribution parameters', *Comput Stat*, vol. 28, no. 4, pp. 1501–1527, Aug. 2013, doi: 10.1007/s00180-012-0364-7.
[28] G. Ribárik, B. Jóni, and T. Ungár, 'The Convolutional Multiple Whole Profile (CMWP) Fitting Method, a Global Optimization Procedure for Microstructure Determination', *Crystals*, vol. 10, no. 7, p. 623, Jul. 2020, doi: 10.3390/cryst10070623.
[29] J. C. Stinville, W. C. Lenthe, M. P. Echlin, P. G. Callahan, D. Texier, and T. M. Pollock, 'Microstructural statistics for fatigue crack initiation in polycrystalline nickel-base superalloys', *Int J Fract*, vol. 208, no. 1–2, pp. 221–240, Dec. 2017, doi: 10.1007/s10704-017-0241-z.
[30] M. A. Charpagne *et al.*, 'Automated and quantitative analysis of plastic strain localization via multi-modal data recombination', *Materials Characterization*, vol. 163, p. 110245, May 2020, doi: 10.1016/j.matchar.2020.110245.
[31] J. C. Stinville, W. C. Lenthe, J. Miao, and T. M. Pollock, 'A combined grain scale elastic–plastic criterion for identification of fatigue crack initiation sites in a twin containing polycrystalline nickel-base superalloy', *Acta Materialia*, vol. 103, pp. 461–473, Jan. 2016, doi: 10.1016/j.actamat.2015.09.050.